Clim Dyn (2012) 38:2227–2242
DOI 10.1007/s00382-011-1171-5

El-Nino Southern Oscillation simulated and predicted in SNU coupled GCMs

Yoo-Geun Ham · In-Sik Kang · Daehyun Kim · Jong-Seong Kug

Received: 18 January 2011 / Accepted: 16 August 2011 / Published online: 26 August 2011

Abstract The characteristics of the El-Nino Southern Oscillation (ENSO) simulated in free integrations using two versions of the Seoul National University (SNU) ocean–atmosphere coupled global climate model (CGCM) are examined. A revised version of the SNU CGCM is developed by incorporating a reduced air–sea coupling interval (from 1 day to 2 h), a parameterization for cumulus momentum transport, a minimum entrainment rate threshold for convective plumes, and a shortened auto-conversion time scale of cloud water to raindrops. With the revised physical processes, lower tropospheric zonal wind anomalies associated with the ENSO-related sea surface temperature anomalies (SSTA) are represented with more realism than those in the original version. From too weak, the standard deviation of SST over the eastern Pacific becomes too strong in the revised version due to the enhanced air–sea coupling strength and intraseasonal variability associated with ENSO. From the oceanic side, the stronger stratification and the shallower-than-observed thermocline over the eastern Pacific also contribute to the excessive ENSO. The impacts of the revised physical processes on the seasonal predictability are investigated in two sets of the hindcast experiment performed using the two versions of CGCMs. The prediction skill measured by anomaly correlation coefficients of monthly-mean SSTA shows that the new version has a higher skill over the tropical Pacific regions compared to the old version. The better atmospheric responses to the ENSO-related SSTA in the revised version lead to the basin-wide SSTA maintained and developed in a manner that is closer to observations. The symptom of an excessively strong ENSO of the new version in the free integration is not prominent in the hindcast experiment because the thermocline depth over the eastern Pacific is maintained as initialized over the arc of time of the hindcast (7 months).

1 Introduction

The last two decades have seen a considerable improvement in the representation of El-Nino Southern Oscillation (ENSO) in the simulations using ocean-atmosphere Coupled General Circulation Models (CGCMs) (e.g., Latif et al. 2001; AchutaRao and Sperber 2002, 2006). According to AchutaRao and Sperber (2006), the frequency and amplitude of ENSO were better simulated by the recent set of CGCMs that participated in the Coupled Model Intercomparison Project Version 3 (CMIP3) as compared to the previous generation models participated in CMIP2. This mainly originated from the improvements introduced in the physical parameterization of CGCMs on the basis of the intensive observations, and the finer resolutions available along with an increase in the computational power over the past few years (Hayes et al. 1991; Zeng et al. 1998; Large

Y.-G. Ham (✉)
Global Modeling and Assimilation Office, NASA Goddard Space Flight Center (NASA/GSFC), Greenbelt, and Goddard Earth Sciences Technology and Research Studies and Investigations, Universities Space Research Association, Building 33, G109, Greenbelt, MD, USA
e-mail: yoo-geun.ham@nasa.gov

I.-S. Kang
School of Earth and Environment Sciences, Seoul National University, Seoul, Korea

D. Kim
Lamont-Doherty Earth Observatory of Columbia University, Palisades, New York, NY, USA

J.-S. Kug
Korea Ocean Research and Development Institute, Ansan, Korea

and Gent 1999; Wu et al. 1998). The wide range of ENSO amplitude represented in the current state-of-the-art CGCMs, however, still prevents a reliable prediction of ENSO in the changing climate (Guilyardi et al. 2009a).

Recent modeling studies showed that the characteristics of ENSO simulated in CGCMs are sensitive to the configurations of the atmospheric component, for example, its cumulus convection scheme (Wu et al. 2007; Kim et al. 2008; Neale et al. 2008; Guilyardi et al. 2009b), and the frequency of air–sea interaction (Danabasoglu et al. 2006; Ham et al. 2009). Neale et al. (2008) demonstrated striking improvements in the ENSO simulation using the Community Climate System Model version 3 (CCSM3). The improvement was achieved by including the convective momentum transport (CMT) scheme and the dilution approximation for the calculation of convective available potential energy in the model. The role of diurnal coupling in the Seoul National University (SNU) CGCM was investigated by Ham et al. (2009). In their study, diurnal coupling weakened the ENSO amplitude by enhancing the atmospheric heat flux damping associated with ENSO.

Separately from model development studies, it has been reported that the predictability of ENSO shown in the dynamical forecasts using CGCMs has been increased, presumably with the aid of the better representation of ENSO in CGCMs. The retrospective ENSO forecasts using the late generations of CGCM showed a superior skill up to three seasons compared to that obtained using the relatively old versions of CGCMs (Barnston et al. 1999; Kirtman et al. 2001; Jin et al. 2008; Wang et al. 2009).

It would be a common wisdom to expect a better prediction skill when using a better model. Such an expectation seems reasonable because a model-error growth during a prediction period would depend on the performance of the model. However, the linkage between the simulation quality of a CGCM in the free integration and the climate predictability using the same model is still not clearly understood. For example, Luo et al. (2005) showed that the SST biases in the free simulations were not systematically related with the ENSO prediction skills. In their study, they performed hindcast experiments using three different versions of a CGCM using different air–sea coupling strategies. Despite of the different biases in SST climatologies that arose from the free integrations, the three versions were similar in the predictability of ENSO.

It seems that a question "Does a CGCM with a smaller error in the free integration have a smaller error in prediction, too?" is not fully answered, and need to be investigated further. To address this issue, we use the two versions of SNU CGCM, one of which has better simulation capability of ENSO than another. We first examine ENSO represented in the free integrations using the two versions. Then we compare the predictability of ENSO obtained from two sets of hindcast experiments. Based on the understanding on the characteristics of the ENSO in the free integrations and the hindcast experiments, we address the following questions;

1. Are the characteristics of ENSO simulated in the free integrations similar to those in the hindcast experiments?
2. Which aspects of the ENSO dynamics are crucial in determining the seasonal predictability of the model?

This paper is organized as follows. Section 2 provides a description of the SNU CGCM, the design of the seasonal prediction experiments, and the observational data used in this study. The tropical Pacific climate and the ENSO characteristics represented in the free integrations of SNU CGCMs are investigated in Sect. 3. Section 4 describes the seasonal prediction skills of the two versions, and Sect. 5 discusses about the role of the oceanic initial conditions on the predicted ENSO. Summary and discussion are presented in Sect. 6.

2 Model, experimental design, and data

2.1 Description of the SNU coupled GCM

The model used in this study is the SNU CGCM (Kug et al. 2008; Kim et al. 2008; Ham et al. 2009). The oceanic part of the coupled model is the Modular Ocean Model (MOM) developed at the Geophysical Fluid Dynamics Laboratory (GFDL). The ocean model (MOM2.2) uses a B-grid finite difference treatment of the primitive equations of motion, Boussinesq and hydrostatic approximations in spherical coordinates, and covers the global oceans with realistic coastlines and bathymetry. The zonal grid spacing is 1.0°. The meridional grid spacing between 8°S and 8°N is 1/3°, gradually increasing to 3.0° at 30°S and 30°N, and it is fixed at 3.0° in the extratropics. There are 32 vertical levels with 23 levels in the upper 450 m with 10 m thickness of the top 10 layers. A mixed layer model, developed by Noh and Kim (1999), is embedded into the ocean model to improve the climatologic vertical structure of the upper ocean.

The atmospheric part of the coupled model is the SNU AGCM, which is a global spectral model at T42 resolution, with 20 vertical sigma levels. The deep convection scheme is a simplified version of the relaxed Arakawa-Schubert scheme (SAS, Numaguti et al., 1995). The large-scale condensation scheme consists of a prognostic microphysics parameterization for total cloud liquid water (Le Treut and Li 1991) with a diagnostic cloud fraction parameterization. A non-precipitating shallow convection scheme (Tiedtke 1983) is also implemented in the model for the midtropospheric moist convection. The boundary layer scheme is a non-local diffusion scheme based on Holtslag and Boville (1993), while the land surface model is from Bonan (1996). Atmospheric radiation is parameterized by a two-stream k distribution scheme as in Nakajima et al. (1995). Other details of the model physics are described in Lee et al. (2001, 2003).

The coupled model exchanges SST, wind stress, freshwater flux, longwave and shortwave radiation, and turbulent fluxes of sensible and latent heat once a day. No flux correction is applied, and the model does not exhibit significant climate drift in the free simulations.

In this study, two different versions of SNU CGCMs are used. We will refer to the version of corresponding to the set-up described above as CGCM Version 1 (V1 hereafter). The next generation of SNU CGCM (Version 2, V2 hereafter) has been developed by revising several physical processes. The differences between V1 and V2 are as follows: (1) the air–sea coupling interval is shortened from 1 day in V1 to 2 h in V2 (Ham et al. 2009), (2) the CMT scheme, as described in Kim et al. (2008), is included in V2, (3) the minimum entrainment rate threshold (Tokioka et al. 1988) is implemented in the convection scheme in V2, and (4) the auto-conversion time-scale of cloud water to raindrops is shortened from 9,600 s in V1 to 3,200 s in V2. The free integrations of the both CGCMs are performed to investigate the performance of the CGCMs. The length of integration is 120 years for the V1, and 50 years for V2. Readers are referred to Kim et al. (2008) and Ham et al. (2009) for the separate impacts of the convective momentum transport and increasing the atmosphere-ocean coupling frequency on the simulation of the tropical Pacific climate and ENSO in this model.

The entrainment rate threshold (Tokioka et al. 1988) implemented in SNU CGCM suppresses convective plumes with entrainment rates less than a threshold value defined as, where D is the planetary boundary layer (PBL) depth and α is a non-negative constant. Therefore, the threshold varies inversely with the PBL depth. The value of α is 0.1 in V2. Inclusion of the minimum entrainment rate threshold in the convection scheme is stimulated by previous studies using atmospheric component of SNU CGCM (Lee et al. 2003; Lin et al. 2008). Lin et al. (2008) showed that the representation of the Madden-Julian oscillation in this model is sensitive to the strength of the convective triggering which the minimum entrainment rate threshold controls.

While the minimum entrainment rate threshold improves the simulation of the subseasonal variability, it causes a cold bias over the entire tropical oceanic regions because it increases the amount of cloud water in the atmosphere thereby reducing downward shortwave radiation at the surface. This side effect from increasing the minimum entrainment rate threshold is remedied in V2 by reducing the auto-conversion time scale for cloud drops to be converted to raindrops. The reduction in the auto-conversion time scale results in faster removal of cloud water in the atmosphere. With this modification, the cold bias over the tropical ocean is reduced, retaining the improvement in the simulated subseasonal variability in V2.

2.2 Seasonal prediction experiment

Seasonal prediction experiments were carried out using SNU CGCM. To obtain initial conditions, the two versions of SNU CGCM were integrated from January 1980 to December 2000 by nudging both the oceanic and atmospheric states toward the reanalysis data. For the oceanic fields, the ocean temperature and salinity fields from the surface to 500 m are nudged toward the Global Ocean Data Assimilation System reanalysis (GODAS, Behringer and Xue 2004) with a 5-day restoring timescale. For the atmosphere, the zonal and meridional wind, temperature, and moisture fields at all vertical levels are nudged toward the ERA-40 Reanalysis of the European Center for Medium-Range Weather Forecasts (ECMWF) (Uppala et al. 2005) using a 6-h restoring timescale. Given the initial conditions, twenty hindcasts with a 7-month lead time were made for the period of 1981–2000, one for each year. The hindcasts have all a start date of May 1 and were stopped on November 30 of the same year. For each hindcast, a four-member ensemble was generated using the Lagged Averaged Forecast (LAF; Hoffman and Kalnay, 1983) method with a 1-day lag. This means that the second (third) ensemble member was generated by starting prediction from April 30 (29), and so on.

2.3 Observational data

For precipitation, we use the monthly-mean data from the Climate Prediction Center (CPC) Merged Analysis of Precipitation (CMAP, Xie and Arkin 1997). The monthly-mean zonal wind stress and daily-mean zonal wind data is from ERA40. The observed SST is from the National Oceanic and Atmospheric Administration (NOAA) Extended Reconstructed Sea Surface Temperatures (ERSST V.2; Smith and Reynolds 2004). The ocean temperature data is obtained from GODAS. The analyzed periods for all observations are from 1981 to 2000.

3 General performance of SNU CGCMs

3.1 Climatological fields

Figure 1 shows the annual-mean SST values simulated in SNU CGCMs and their biases from observations over the equatorial domain. Both model versions show a well-developed equatorial cold tongue along the equator over the eastern Pacific. The equatorial cold tongue simulated in V1 extends westward more than that observed as in many other CGCMs (Wittenberg et al. 2006), due to the equatorial SST bias approaching −2°C in the central Pacific. The SST bias over the central Pacific in V2 is less than 1°C in magnitude and thus is smaller than that of V1. The reduction of the cold bias over the central Pacific is possibly due to the reduced climatological low-level easterly winds (Fig. 2) and the associated reduction of equatorial upwelling, which induces the weaker extension of cold tongue water. The reduction of the cold bias from V1 to V2 is larger than that in Kim et al. (2008) and Ham et al. (2009), where the reduced cold bias due to CMT and the diurnal coupling was reported. This suggests that the additional physical processes other than CMT and the enhanced air–sea coupling frequency in V2 play a positive role in reducing the cold bias. The mean warming in V2 compared to V1 is accompanied by a reduction in the amplitude of the mean annual cycle of SST over the equatorial Pacific, towards more realistic values especially east of the dateline (not shown). The strong and erroneous westward propagation of SSTs in the western half of the basin that is apparent in V1 is no longer present in V2. In both model versions, the spring warming is delayed by 1–2 months with respect to observations.

Figure 2 shows the annual-mean precipitation and zonal wind at 850 hPa from observations as well as those simulated in V1 and V2. In observations, the pattern of mean precipitation over the equatorial Pacific is characterized by one centre over the north-western Pacific, another centre over the south Pacific convergence zone (SPCZ) and the zonally elongated rain band over the central-to-eastern Pacific, called intertropical convergence zone (ITCZ). These features are generally well captured by both versions. Compared to observations, however, V1 shows a weaker precipitation over the equatorial central Pacific and eastern Indian Ocean, while displaying wet biases over the maritime continents and western Indian Ocean. These precipitation biases are largely coincident with the local SST biases; there are dry biases over the western-central Pacific and Indian Ocean where cold biases exist (Fig. 1). On the other hand, V2 has a wet bias over the equatorial central Pacific where the SST bias is nearly zero, and dry bias over the equatorial western Pacific. In addition, in both V1 and V2 the SPCZ extends further to the East than in observations. This reflects the ‘double ITCZ’ bias in SNU CGCM, the problem that is common in the state-of-the-art CGCMs (Lin 2007).

The negative precipitation bias over the central to eastern Pacific in V1 enhances the east-west asymmetry in precipitation along the equator, resulting in the Walker circulation whose strength is stronger than that observed. This is reflected in the stronger trade winds over the equatorial Pacific seen in Fig. 2. The excessive climatological easterly winds, which might cause the cold bias over the equatorial central Pacific through excessive easterly ocean currents and upwelling in the V1, is reduced in V2. The climatological easterly wind over the central

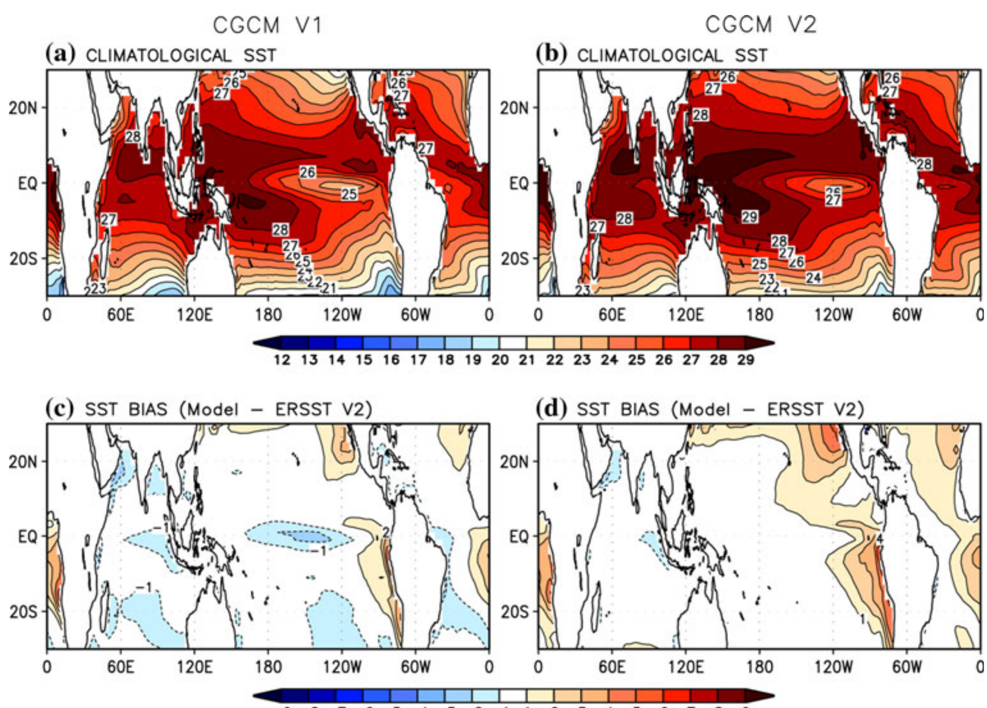

Fig. 1 Free integration simulation results of annual-mean SST (°C) in **a** CGCM V.1, and **b** CGCM V.2. **c**, **d** Biases of climatological SST from ERSST V.2

Pacific in V2 is around -8 m/s, which is close to observed values. We attribute the reduction in the cold bias in V2 to the reduction in the equatorial easterly winds.

To investigate causes of the difference between V1 and V2, additional experiments were performed using the atmospheric components of two versions. Two versions of atmospheric GCM (AGCM) are integrated for 4 years (1999–2002) by prescribing observed SST as a boundary condition. Because the boundary condition is same, any difference between the two versions in the AGCM experiment is caused solely by the difference in the atmospheric model. Figure 3 shows the difference map of the climatological 850 hPa zonal wind and surface downward shortwave radiation between two AGCM experiments. The results from the AGCM experiments show that the low-level westerly winds over the western Pacific increases dramatically with changes from V1 to V2. Over the central Pacific, however, the magnitude of changes is small, and the sign is opposite to that in the CGCM experiments. This suggests that the oceanic responses to the atmospheric physics changes, and ocean-atmosphere coupled feedback processes play a major role in reducing the climatological easterly winds over central Pacific in V2.

Although the mechanism responsible for the changes in the climatological low-level zonal wind in CGCM experiments is not clear in this stage and need to be investigated further, one possibility is that the warming over the Pacific, especially the eastern part of it, can feed back to atmosphere to reduce the strength of the Walker circulation. Figure 3b shows that there is a global increase of the surface downward shortwave radiation over the tropics. The increase of the shortwave radiation at the surface stems from the reduction in the auto-conversion rate, which reduces the amount of cloud liquid water in the air. Even though the amount of shortwave increase caused by the reduced auto conversion rate is similar over the entire Pacific, the resultant SST warming would be larger over the eastern Pacific than in other regions, because of the smaller effective ocean heat contents in that region. Then, the relatively significant warming over the eastern Pacific may reduce the Walker Circulation through the Bjerkness feedback, and the anomalous surface westerly winds over the Pacific reinforces the SST warming by deepening the equatorial thermocline through the Ekman transport and reduced upwelling.

Figure 4 shows the simulated Pacific upper-ocean temperatures along the equator, with the bias compared to the GODAS data. The overall structure of the thermocline is well captured in both model versions, although the vertical temperature gradient near the thermocline is smaller than that observed in both versions (not shown). In both versions, the vertical temperature gradient is stronger than that observed over the far eastern Pacific, where the mixed layer depth is relatively shallow, with a warm surface bias sitting directly above a cold subsurface bias around 50-100 m. There is a cold bias along the thermocline, which approaches about 5°C in V1. The magnitude of the cold bias is reduced in V2 (about 3°C), when compared to V1.

The reductions in the cold biases at the surface and subsurface in V2 are caused by the reduced easterly winds (Fig. 2), which deepen the equatorial thermocline through changes in Ekman transport. The anomalous downwelling caused by reduced Ekman transport leads to a maximum

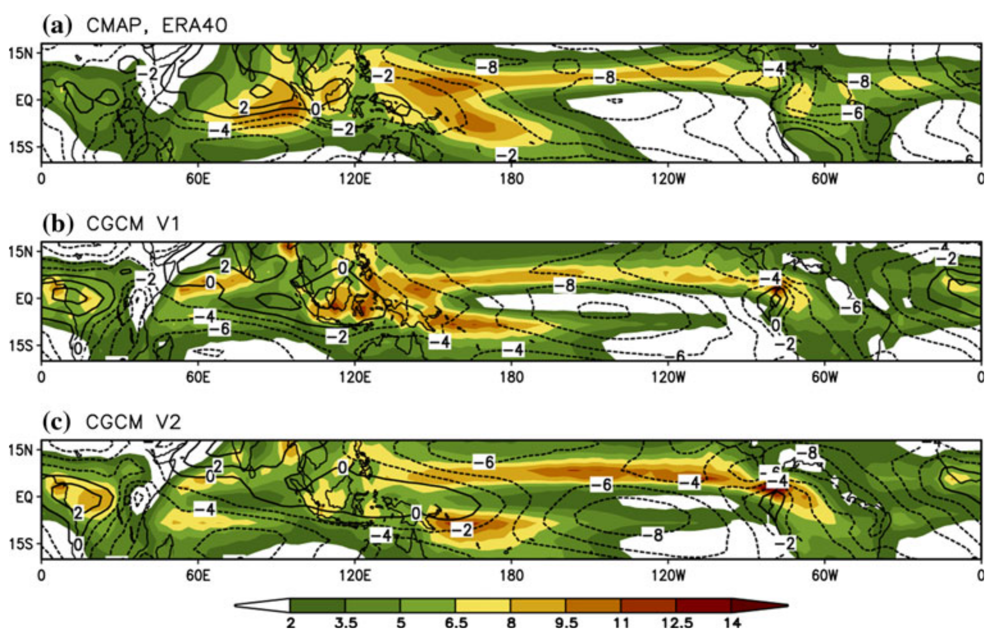

Fig. 2 Climatological precipitations (shading, in mm/day) and zonal winds at 850 hPa (contours, in m/s) in **a** CMAP and NCEP/NCAR reanalysis, and **b** free integration of CGCM V.1 and **c** CGCM V.2. Note that the CMAP and ERA40data are used as validating observations. Note that the positive value in zonal winds denotes the westerly winds

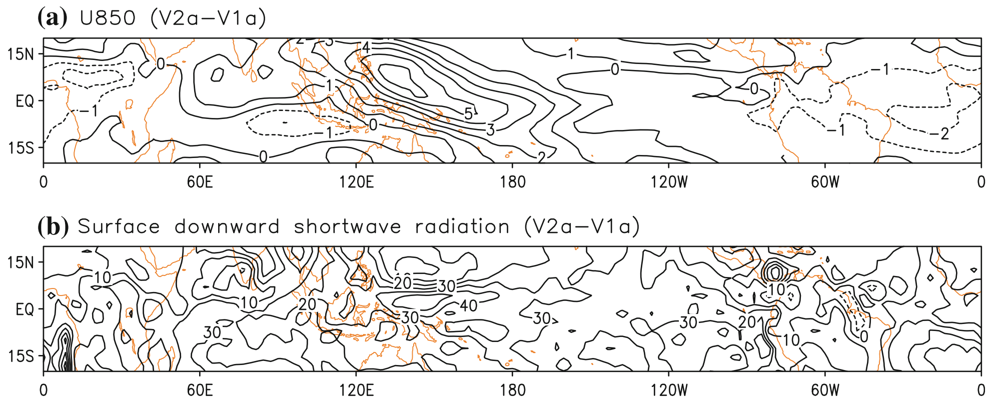

Fig. 3 The difference map of **a** the climatological 850 hPa zonal wind (unit: m/s) and **b** surface downward shortwave radiation (unit: W/m^2). Atmospheric component of the V1 and V2 were integrated for 4 years (1992–2002) with observed SST as a lower boundary condition. The difference stands for V2a–V1a, where V2a (V1a) represents atmospheric component of CGCM V2

Fig. 4 Free integration results of climatological subsurface temperature in °C averaged over equatorial regions (5°S–5°N) in **a** CGCM V.1 and **b** CGCM V.2. **c**, **d** Biases of climatological subsurface temperature from observations (GODAS)

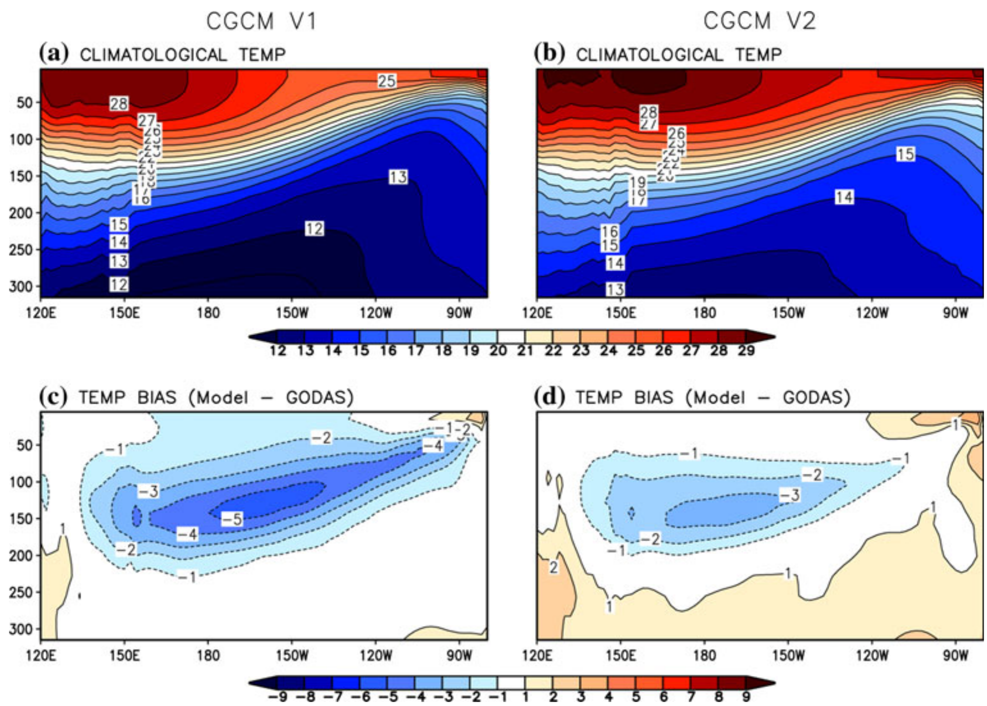

warming at the depth of the thermocline, where the vertical temperature gradient is largest. Because the western Pacific westerlies lead to a rise in the zonal mean equatorial sea level and a deepening of the thermocline, they also partly contribute to the reduction in the cold biases over the whole Pacific domain in V2.

3.2 ENSO characteristics

The characteristics of ENSO simulated in the free integrations using two versions will be shown in this subsection. The difference between two versions will be addressed on the basis of the theoretical frameworks. The understanding we obtain in this section will be used to interpret the characteristics of ENSO in the hindcast experiments in the following section.

Figure 5 shows the standard deviation (SD) of the monthly-mean SST anomalies. The overall structures of the SST variability in the observations are well captured in both versions. However, in V1, the ENSO-related SST anomaly is weaker than that in the observations. In addition, the SST variability in V1 is meridionally narrower than that observed. In V2, the SD of SST anomaly is about twice that in the observations. For example, the maximum SD value in V2 is over 2°C, while that in the observations is about 1.2°C. In both versions, the longitudinal maximum of the SST anomaly is shifted westward by about 20° compared to that observed. Note that the westward shift of the SST variability during ENSO is a common symptom in the current state-of-the-art CGCMs (AchutaRao and Sperber 2002; Davey et al. 2002; Latif et al. 2001; Kug et al. 2010).

Figure 6 shows the SD of the Nino3.4 index (SST anomaly averaged over the boxed area: 170°W–120°W, 5°S–5°N) for each calendar month. To investigate the seasonal difference of the Nino3.4 index magnitude, the Nino3.4 index is normalized by the SDs calculated using data from whole period. The observed Nino3.4 SST anomalies tend to have a maximum variance during boreal winter and a minimum in boreal spring. Overall, both versions simulate this feature well. However, the peak variance of the Nino3.4 index in V1 appears about 1 month later than the observed, and the variance is rather flat in the boreal autumn and winter. This means that the seasonal locking is poorly simulated in V1. This deficiency is not seen in V2.

Figure 7 shows the spectra of Nino3.4 indices from observations and simulations, to compare the dominant frequency in the variability. Similar to the Fig. 6, the Nino3.4 index is normalized by the SD calculated using data from the whole period. The observations show spectral peaks in the interannual band at 2.5, 4, and 5 years. In V1, the spectral peak of ENSO is relatively lower than observed. The spectral peak of ENSO in V1 is at about 2.5 years, and there is no spectral peak at around 5 years. On the other hand, V2 captures the 4–5 year period of ENSO, as well as its biennial behavior.

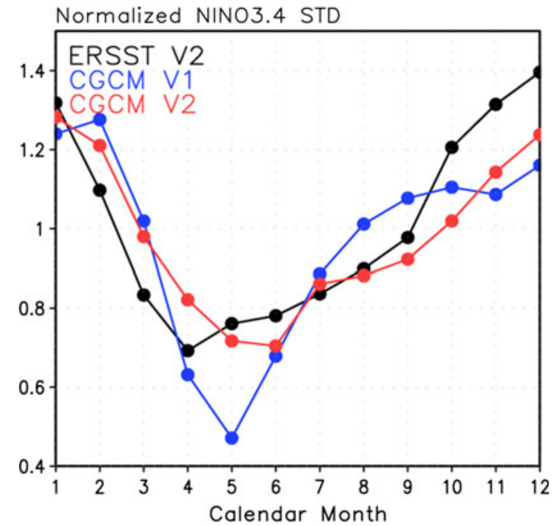

Fig. 6 The standard deviation of monthly-mean Nino3.4 index for each calendar month in free integration of model simulations (*red* for CGCM V.2 and *blue* for CGCM V.1) and observations (ERSST V.2, *black*). To focus on the seasonal difference of Nino3.4 variability, Nino3.4 index is normalized based on its standard deviation using whole period

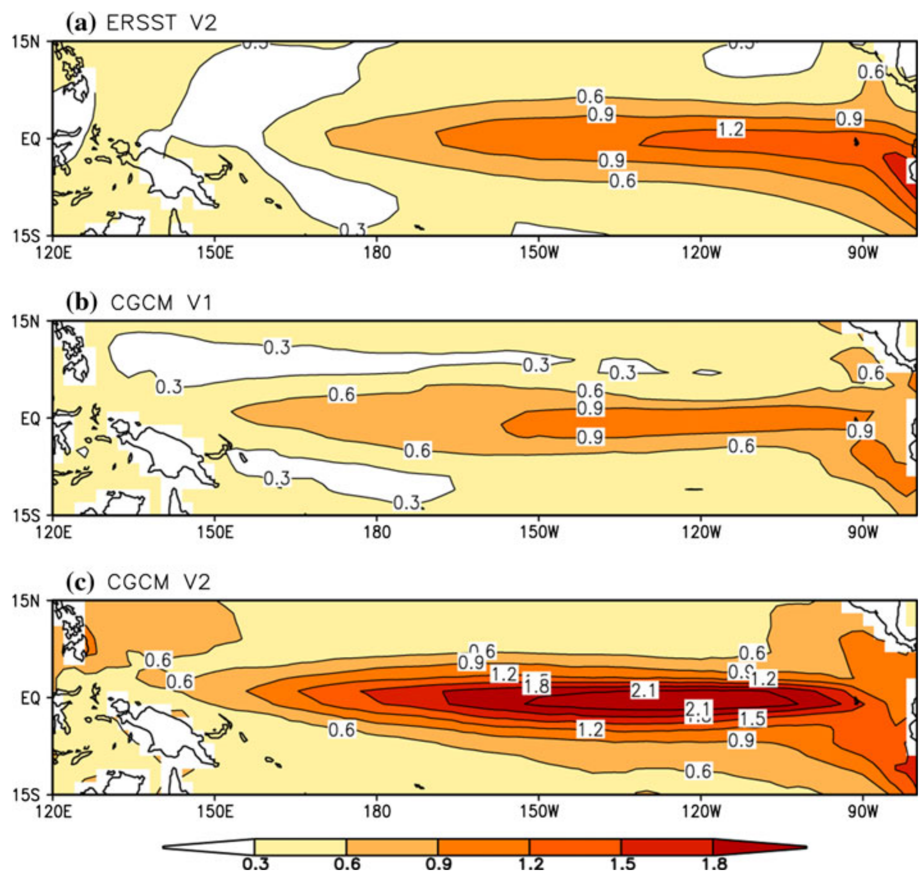

Fig. 5 Spatial patterns of standard deviation (unit: °C) of monthly-mean SST anomalies in **a** observations (ERSST V.2), and free integration of **b** CGCM V.1 and **c** CGCM V.2

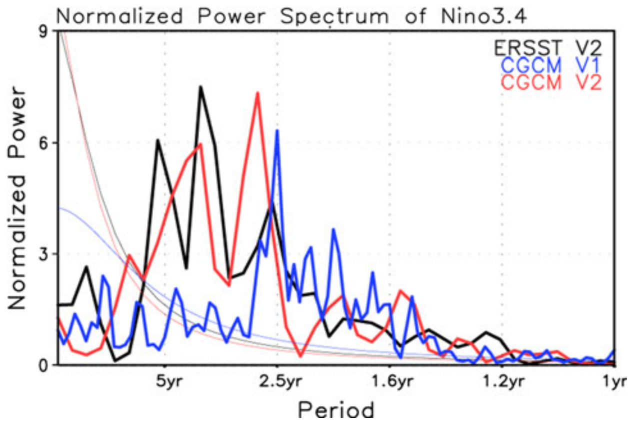

Fig. 7 Power spectra analysis of normalized monthly-mean Nino3.4 index using free-integration results of SNU CGCMs (*red* for CGCM V.2 and *blue* for CGCM V.1), and observations (ERSST V.2, *black*)

The longer period ENSO in V2 is related to the improved simulation of the ENSO-related atmospheric fields. Figure 8 shows the spatial patterns of the zonal wind stress anomaly regressed onto Nino3.4 in the observations, V1 and V2. The ENSO-related zonal wind stress anomaly is the strongest in the observations, at about 0.2 N/m^2/°C over the central Pacific. Even though the zonal location of the regressed zonal wind stress is well simulated in both versions, the magnitude is too weak in V1. On the other hand, the magnitude of the regressed zonal wind stress is about 0.1 N/m^2/°C in V2. Jin (1997) showed that a stronger air–sea coupling strength led a stronger ENSO with a longer period in the simple conceptual model. His work supports our results in that the version with the stronger air–sea coupling strength shows the frequency (magnitude) of ENSO longer (stronger) than that in the version with a relatively weaker coupling strength. The meridional width of the zonal wind stress anomaly is wider and closer to observations in V2. Along with the air–sea coupling strength, the meridional widening of the zonal wind stress anomalies tends to produce the longer period ENSO, by slowing the oceanic adjustment via oceanic Rossby waves (Cane et al. 1990; Kirtman 1997; An and Wang 2000; Kang and Kug 2002; Kug et al. 2003).

The improved simulation of the ENSO-related wind stress anomaly is mainly the result of the CMT parameterization (Kim et al. 2008). According to Kim et al. (2008), the CMT parameterization is designed to represent a ‘two-way’ transport of momentum between upper and lower levels in the atmosphere, which communicate with each other via CMT in regions of strong vertical wind shear and convective activity. It implies the upper level westerly winds is transported to a low-level over the convective activity related to the El Nino, therefore the low-level westerly wind anomalies over the central Pacific are enhanced. It means the weak westerly wind stress anomaly is enhanced over the central Pacific during the El Nino, and it leads longer and stronger ENSO when CMT parameterization is included.

In addition to the fluctuation of monthly-mean fields related to ENSO, it is also shown in the observations that the subseasonal variability is intensified during the development phase of ENSO over the western Pacific (McPhaden and Taft 1988; Vecchi and Harrison 2000; McPhaden 2002). Along with the observational evidence, model experiments support the conclusion that Westerly Wind Events (WWEs) over the western Pacific can bring warming to the eastern Pacific after several months. Kessler and Kleeman (2000) showed that several nonlinear processes, such as high-frequency winds, evaporation, vertical temperature gradient, and zonal currents, can lead to the SST warming over the central-eastern Pacific. In addition, Vecchi and Harrison (2000) argued that the WWEs trigger an eastern equatorial Pacific warming, associated with the generation of the equatorial downwelling Kelvin waves.

To investigate the ENSO-related high-frequency (HF) wind activity, Fig. 9 shows the lag correlation between the anomalous subseasonal (2–90 day filtered) variance of zonal wind at 850 hPa over the equator (5°S–5°N) and the Nino3.4 index in the CGCM simulations and observations. The lag correlation between the monthly-mean 850 hPa wind anomalies and the Nino3.4 index is also shown, because the westerly monthly-mean wind anomaly is closely linked to the subseasonal wind variability (Seiki and Takayabu 2007; Sooraj et al. 2008). In the observations, enhanced HF wind activity and westerly monthly-mean wind anomalies occurs from 12 months prior to the ENSO peak season (McPhaden, 1999). From 12 months prior to the El Nino peak phase, the positive HF wind activity propagates from the western to central Pacific. This feature is well captured in V2, even though the amplitude of the positive HF wind activity is larger than the observations. The El Nino-related HF wind activity barely occurs in V1, suggesting an additional argument why V1 simulates weaker El Nino than that in V2 and observations.

It has been shown so far in this section that the atmospheric response to the El Nino is more realistic in V2 than that in V1. To investigate the oceanic role, we evaluate two dominant oceanic feedback processes, the zonal advective and the thermocline feedback (An and Jin 2001; Jin and An 1999; An et al. 1999, 2008). The former results from the SST tendency due to the climatological zonal SST gradient and the anomalous westerly current there (i.e. $-u'\frac{\partial \overline{T}}{\partial x}$), and the later results from the SST tendency due to the climatological upwelling and the anomalous vertical temperature gradient there (i.e. $-\overline{W}\frac{\partial T'}{\partial z}$). In observations, both feedbacks warm up the eastern Pacific SST during the development of El Nino events (Fig. 10a).

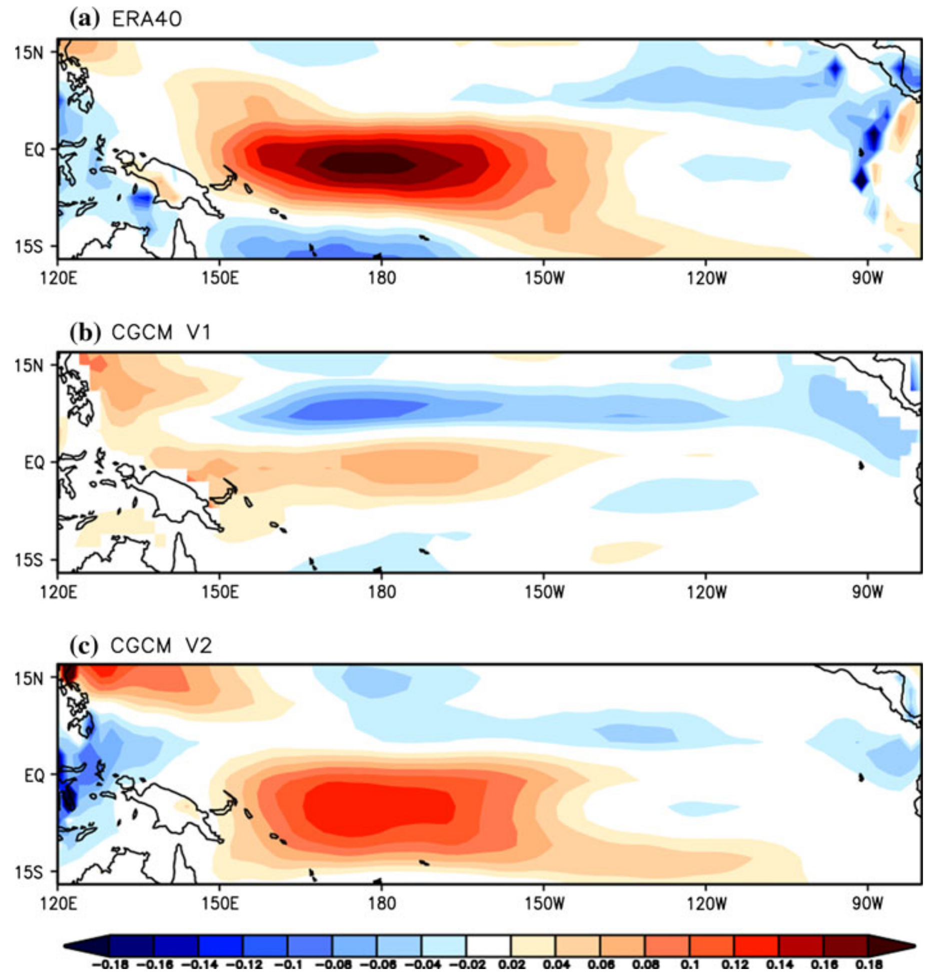

Fig. 8 Monthly-mean zonal wind stress anomalies regressed onto Nino3.4 index (unit: N/m^2/°C) in **a** observations (ERA40), and free integration of **b** CGCM V.1 and **c** CGCM V.2. Note that it provides the magnitude of zonal wind stress anomaly with respect to unit change of Nino3.4 index. ERSST V.2 is used to obtain observed Nino3.4 index

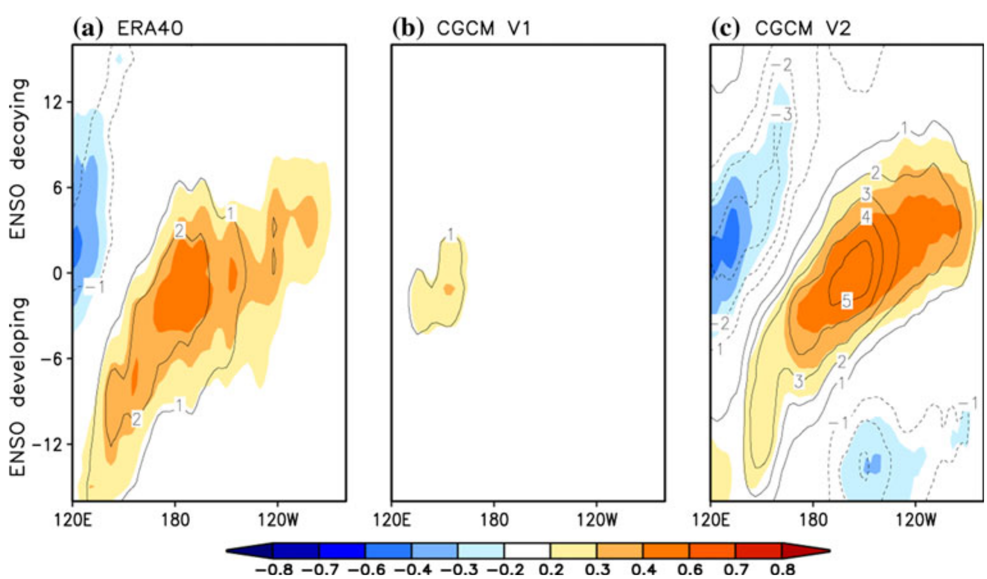

Fig. 9 Lag correlation between Nino3.4 index and monthly-mean anomalies of 850 hPa zonal winds over equatorial region (5°S–5°N) (*contour*, in m/s/°C), and between Nino3.4 index and anomalous subseasonal (2–90 day filtered) variance of zonal wind at 850 hPa (*shading*, in m^2/s^2/°C) in **a** observations (ERA40), and free integration of **b** CGCM V.1 and **c** CGCM V.2. The positive (negative) values on the y-axis indicate the lead/lag month that the Nino3.4 index leads (lags) the zonal winds. Note that the observed Nino3.4 index is obtained using ERSST V.2

To investigate the relative importance of the thermocline and zonal advective feedback, Fig. 10 shows the lead-lag regression of the temperature advection terms related to the zonal advective feedback and thermocline feedback against the Nino3.4 index. Note that the zonal current, mean temperature anomaly, and mean vertical velocity is averaged from 0 to 50 m, and the vertical temperature gradient is calculated based on the difference between SST

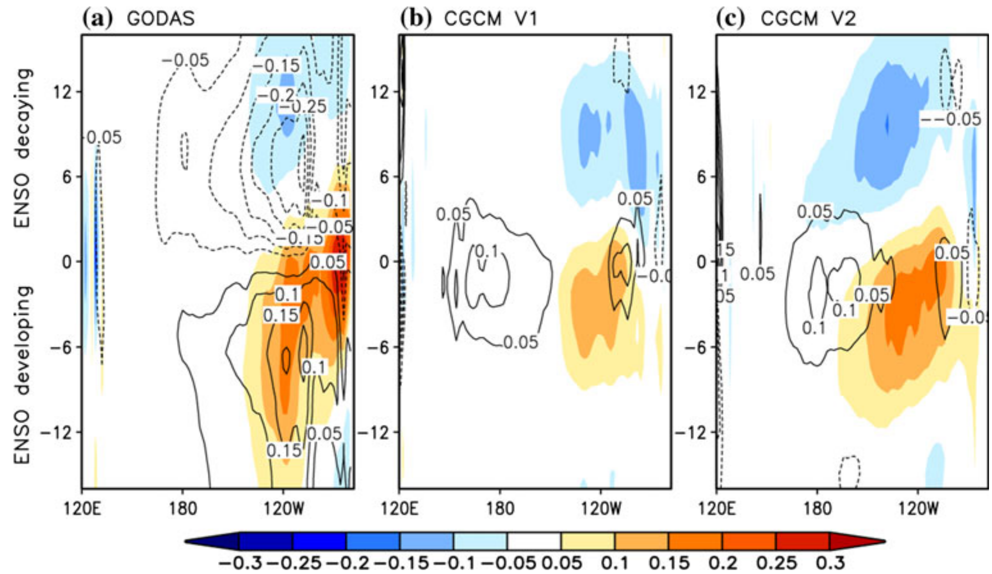

Fig. 10 Lead-lag regression between equatorial (5°S–5°N) monthly-mean vertical advection of anomalous temperature caused by climatological upwelling (*shading*, $-\overline{W}\frac{\partial T'}{\partial z}$), monthly-mean zonal advection of mean temperature caused by anomalous zonal currents (*contour*, $-u'\frac{\partial \overline{T}}{\partial x}$), and Nino3.4 index in **a** observations (GODAS), and free integrations of **b** CGCM V.1, and **c** CGCM V.2. Note that the positive (negative) values on the y-axis indicate that the Nino3.4 index leads (lags) the advection terms. The y-axis unit is the month. The unit is °C/month/°C, therefore, it provides the magnitude of advection with respect to unit change of Nino3.4 index

and the temperature at 50 m. The unit of the advection is the time tendency of the temperature per unit SST change (°C/month/°C).

In V1, the magnitudes of both feedbacks, which are known to be important to the evolution of ENSO, are weaker than those observed. In addition, the magnitude of the zonal advective feedback is at its maximum during the ENSO peak phase. This means the simulated zonal advective feedback is not responsible for the evolution of the SST anomalies. On the other hand, the temperature tendency from the vertical advection is positive (negative) during the ENSO evolution (decaying) phase. This implies that the thermocline feedback is responsible for the evolution of ENSO in V1. In V2, The zonal advective feedback is still in-phase with the SST anomalies, while the thermocline feedback is in-phase with the SST tendency. The magnitude of the thermocline feedback in V2 is increased by about 50% compared to that in V1, while that of the zonal advective feedback remains similar. Above results suggest that the thermocline feedback is a key process for the ENSO-related SST anomalies in the models.

The stronger-than-observed ENSO magnitude in V2 may be due to the stronger climatological vertical temperature gradient than that in observations. An and Jin (2001) showed that the growth of ENSO is stronger when the climatological vertical temperature gradient is larger, as a result of intensified thermocline feedback. As shown in Fig. 4, the climatological SST is warmer by about 2°C in V2 than in the observations, On the other hand, the climatological subsurface temperature is cooler than that in observations by about 2°C over the eastern Pacific regions. To examine the climatological vertical temperature change in more detail, the temperature difference between surface and 50 m over the equatorial eastern Pacific (180°E–90°W, 5°S–5°N) is calculated. As expected, the vertical temperature gradient over the eastern Pacific is stronger in V2 (1.87°C) than that in observations (1.08°C). Hence, the differences in the oceanic mean states may lead the stronger ENSO in V2.

In addition, the cold bias of the subsurface temperature in V2 implies that the simulated climatological thermocline depth is shallower than that observed. This shallower thermocline depth leads to the stronger ENSO magnitude, because isotherm vertical displacements can more easily influence SST (Jin and An 1999; An and Jin 2001; Yeh et al. 2009). This implies that simulations of the stronger climatological vertical temperature gradient and shallower climatological thermocline depth in V2 may lead to the excessive ENSO compared to that observed.

4 ENSO predictability

Two sets of the hindcast experiments are performed using the two versions of the CGCM. Prediction skills of the two versions of the model in the Indo-Pacific regions are illustrated in Fig. 11, through the anomaly correlation maps of September–November averaged SSTA against their observed counterparts. The correlation coefficient is generally higher over the north-central and southwestern Pacific regions than that over other regions, with relative minimum near the equatorial eastern Pacific. The minimum over the equatorial Pacific is less prominent in V2. In V2, there is the area over the central Pacific where the correlation coefficient is over 0.8, while such an area is hardly seen in V1. Overall, V2 has more skill than that in V1 in predicting SST anomaly over the tropical Pacific.

Figure 12 shows the anomaly correlation coefficients of the various ENSO indices as a function of the prediction lead month. It is clear that the correlation coefficients of the various ENSO indices are higher in V2 than those in V1. For example, the correlation coefficient of the NINO3.4 index in the V1 hindcast is about 0.7 at a 6-month lead time, while that in the V2 hindcast is over 0.8. Among them, the correlation skill improvement is most robust over the NINO4 region.

One can wonder why the prediction skill of V2 is better than that of V1, because the magnitude of ENSO simulated in the free integration of V2 is excessive than that in observation, which might degrade the forecast skill. Interestingly, the stronger-than-observed ENSO in the free integration of V2 (Sect. 3b) does not occur in the hindcast experiments. The SD of the Nino3.4 index for the hindcasts is 0.77 in V2, which is smaller than the observed (i.e. 0.87). In addition, the SD in V1 becomes weaker (i.e. 0.62) than that in the free integration (i.e. 0.68). The reason for this weaker ENSO magnitude in the hindcast experiments will be discussed later.

The weaker ENSO magnitude in V1 implies that ENSO predicted using V1 is damped out more quickly than they should be, and this degrades the prediction skill. Figure 13 shows the composites of the temperature anomalies during the La Nina years (1984, 1988, and 1999) for the simulations and observations. Note that we focused on La Nina events, because the predicted Nino3.4 index in V1 is especially weaker during the La Nina events than that during El Nino events (not shown). In the observations, the negative SST anomalies are retained until the 7-month lead time, while those in V1 are damped as soon as the prediction starts. On the other hand, in V2, the negative temperature anomalies associated with the La Nina events are maintained up to 6-month lead time with magnitudes similar to that observed. This feature is especially clear in the 100-m temperatures. In V1, the negative 100-m temperature anomaly is abruptly damped, and the temperature anomalies are nearly zero after 4 months. However, the negative temperature anomalies in V2 prediction and observations are sustained until the 7-month lead time. This implies that ENSO in the hindcast experiment using theV1

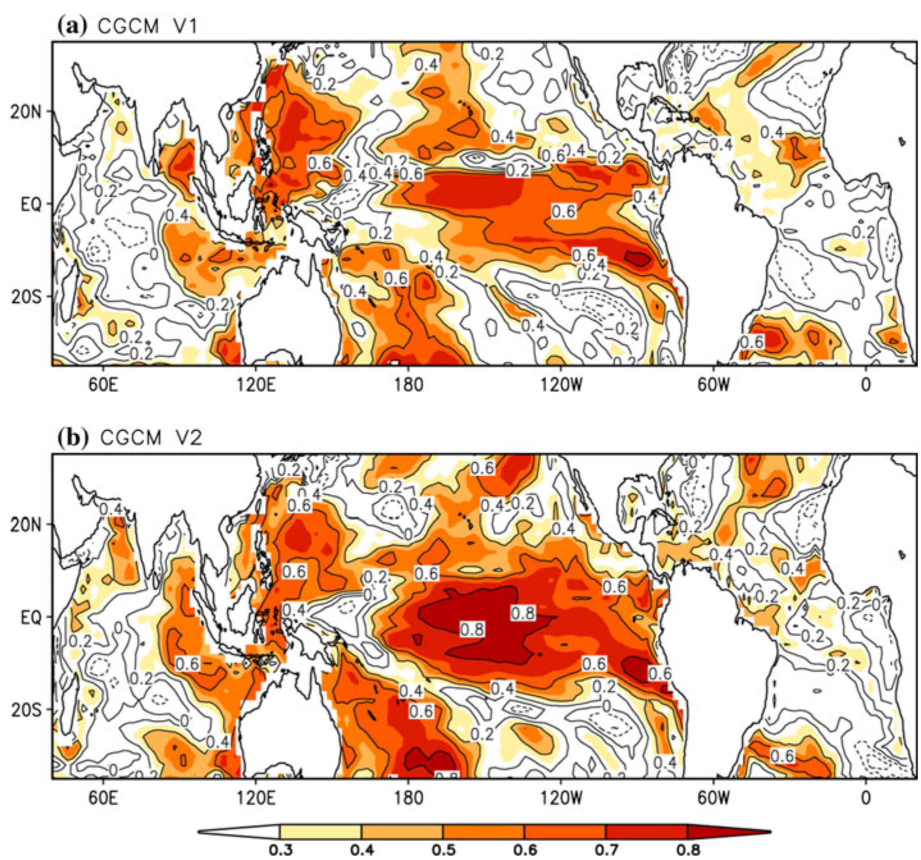

Fig. 11 Correlation coefficients of SON SST anomalies of **a** SNU CGCM V.1 and **b** CGCM V.2 with respect to the observations. Note that ERSST V.2 are used as validating observations

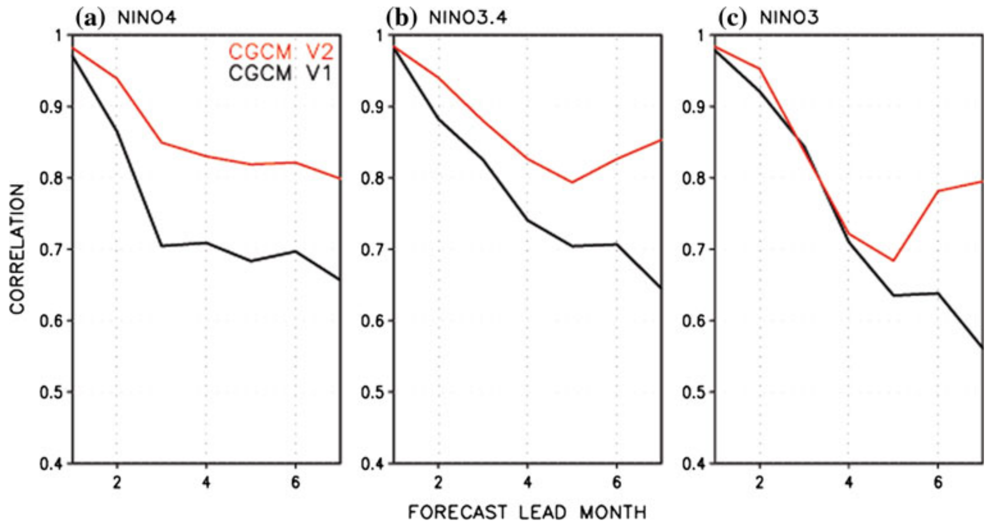

Fig. 12 Correlation coefficients of monthly-mean **a** Nino4, **b** Nino3.4, and **c** Nino3 indices with respect to forecast lead month in prediction experiments with SNU CGCMs. Note that ERSST V.2 are used as validating observations

quickly damps, which lowers the predictability of ENSO in V1.

5 Role of oceanic initial conditions on predicted ENSO magnitudes

To understand the difference between the ENSO magnitudes simulated in the free integrations and that predicted in the hindcast experiments using V2, it is worthwhile to compare the atmospheric feedback (i.e. air–sea coupling strength) and the thermocline feedback in the free integrations and the hindcast experiments, as investigated in Sect. 3. As a metric for the strength of the thermocline feedback, the climatological thermocline-depth (defined as 20°C isotherm line) averaged over 160°E–90°W, 5°S–5°N (Z20 hereafter) is chosen, because the climatological thermocline depth is a proxy for the strength of thermocline feedback. For example, when Z20 is too shallow, vertical temperature gradient is reduced, therefore it stabilizes the thermocline feedback (Bejarano and Jin 2006). Note that the air–sea coupling strength is the anomalous area-averaged zonal wind stress (160°E–150°W, 5°S–5°N) regressed onto the Nino3.4 index.

Figure 14 shows a scatter diagram for the climatological Z20 (x-axis) and the air–sea coupling strength (y-axis) during June-August in the free integrations and the hindcast experiments, along with the observations. It is clear that the climatological Z20 in the hindcast experiments is deeper than that in the free integrations. For example, the Z20 values of V1 and V2 in the hindcast experiments are about 108.3 m and 106.1 m, while those in the free integrations are 83.3 and 97.5 m, respectively. The climatological Z20 in the hindcast experiments is more similar to the observed value of 113 m. The increase of Z20 in the hindcast experiments suggests that the ENSO magnitude in the hindcast experiments can be smaller than that in the free integration due to the reduced strength of the thermocline feedback. On the other hand, the air–sea coupling strength in the hindcast experiment is almost same to that in the free integration. For example, the air–sea coupling strength is about 0.08 (0.05) N/m^2/°C both in the free integrations and the hindcast experiments using V2 (V1). It is worthwhile to noting the climatological Z20 follows the observed values up to one season, while the air–sea coupling strength does not. This implies that the model deficiencies in the ocean do not seem to overwhelm the initialized fields at least up to one season, while the atmospheric characteristics in the hindcast experiments shortly converges to the model's inherent characteristics.

As a prediction begins, the impact of the initial conditions lasts for a while, but the characteristics of the prediction should eventually converge to that of the model performance. The time scale of this convergence is expected to be different for the atmosphere and the ocean. For example, the impact of the oceanic initial conditions lasts up to several months, which means the oceanic states in the hindcast experiments follow those of the observations for up to several months. However, the impact of the atmospheric initial conditions lasts at most 1–2 weeks, so that the characteristics of the atmospheric in a seasonal prediction are similar to those of the free integration.

To investigate how long the oceanic and atmospheric fields are influenced by the initialized fields, Fig. 15 shows the climatological Z20 and the air–sea coupling strength in observations, the hindcast experiments and free integrations. In the hindcast experiments using V1 (blue solid line in Fig. 15a), Z20 is closer to the observations rather than to the free integration. For example, the difference of Z20 between the hindcast experiment and observations is about

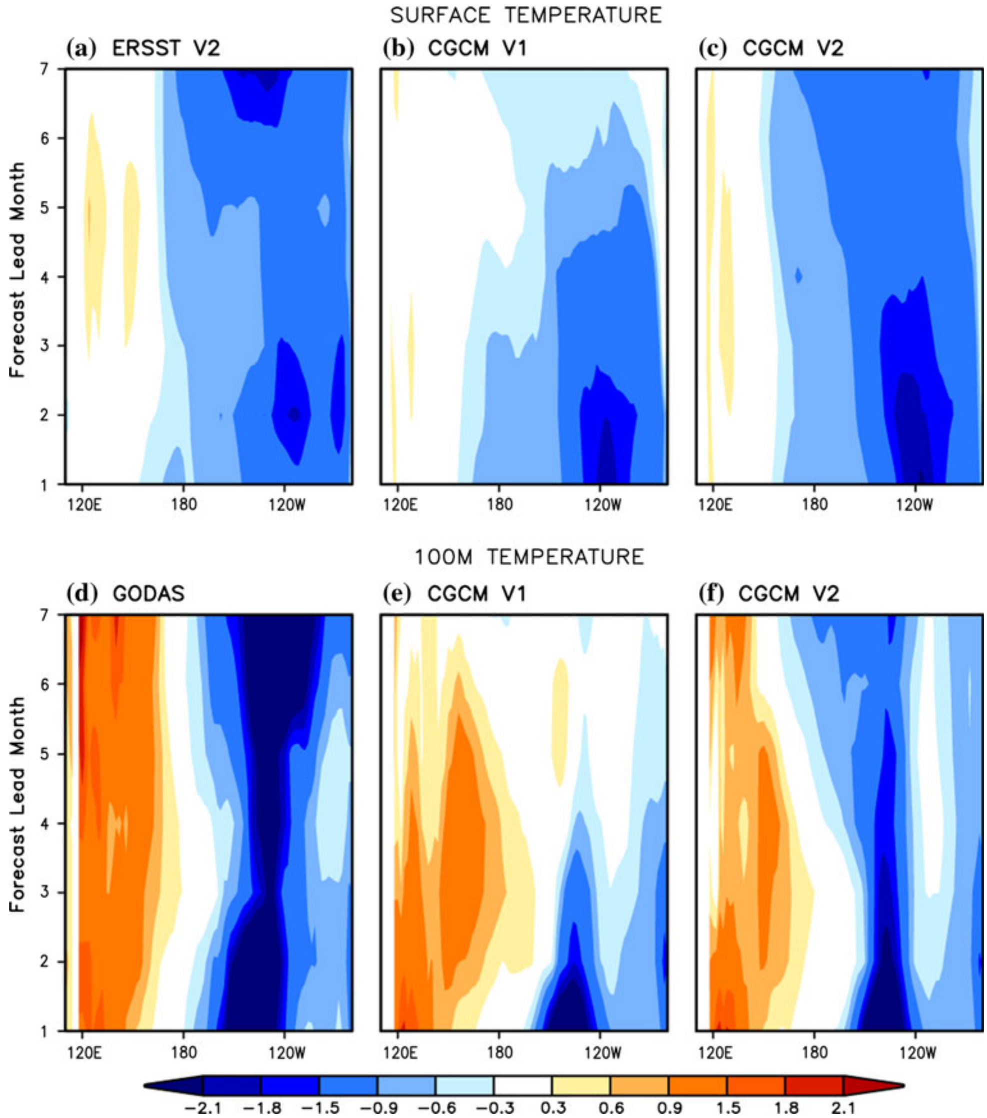

Fig. 13 Composite of monthly-mean equatorial SST (*upper panel*), and 100-m subsurface (*lower panel*) anomalies (unit: °C) during La Nina seasons (1984, 1988, and 1999) with respect to forecast lead month in both prediction experiments and observations. Note that the 5°S–5°N averaged values are shown. Note that ERSST V.2 and GODAS are used as validating observations

10 m, while that between the hindcast experiment and the free integration is about 30 m. Similarly, Z20 in the hindcast experiments using V2 are influenced by the initial condition up to 4 prediction lead month. However, the air–sea coupling strength in the hindcast experiment is similar to that in the free integrations rather than that in observations at 3 prediction lead month. It shows that the oceanic simulation in the hindcast experiments is influenced by the initial condition up to several months, while the atmospheric simulations in the hindcast experiments converge to that in the free integration within few weeks.

Because the air–sea coupling strength is more realistic in V2, the seasonal prediction with V2 shows a more realistic ENSO magnitude with the aid of the realistic atmospheric responses. However, the seasonal prediction with V1 shows a smaller ENSO magnitude because of the weak air–sea coupling strength, even though the oceanic state is realistic as a result of the constraint of the initial conditions. The weak air–sea coupling strength in V1 damps out the ENSO signals faster than it should be, thus degrades the prediction skills.

6 Summary and conclusions

In this study, the simulation of the tropical Pacific climate and ENSO is investigated using two versions of SNU CGCM, and the possible linkage between the performance in the free integrations and the seasonal prediction skill is discussed.

A revised version of SNU CGCM is formulated by reducing the air–sea coupling interval from 1 day to 2 h,

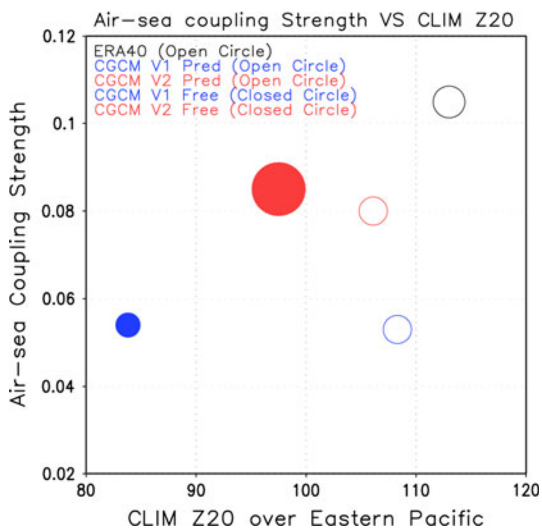

Fig. 14 Scatter diagram between climatological thermocline depth (x-axis) and air–sea coupling strength (y-axis) in observations (*black circle*), and prediction (*open circle*) and free integrations (*filled circle*) experiments of the V1 (*blue*), and the V2 (*red*) during JJA. The size of each *circle* is proportional to the standard deviation of monthly-mean Nino3.4. Note that the climatological thermocline depths are averaged values over 160°E–90°W, 5°S–5°N, and the air–sea coupling strength is the anomalous area-averaged zonal wind stress (160°E–150°W, 5°S–5°N) regressed onto the Nino3.4 index

including the parameterization of CMT and the minimum entrainment rate threshold in the convection scheme. In addition to these modifications, the auto-conversion time scale of cloud water to raindrops was shortened. In the new version (V2), the surface and sub-surface temperature biases over tropical Pacific are reduced, and the structures of the ENSO-related atmospheric anomalies over the tropical Pacific becomes more realistic compared to the previous version (V1). In particular, the simulation of the ENSO-related anomalous zonal wind stress and sub-seasonal variability are improved, even though the standard deviation of the SST anomalies over the eastern Pacific in the new version is too strong. The stronger standard deviation of SST over the eastern Pacific in the revised version is due to the stronger stratification and the shallower-than-observed thermocline over the eastern Pacific as well as the enhanced air–sea coupling strength and intraseasonal variability associated with the ENSO.

With the aid of the realistic ENSO-related atmospheric anomalies, the seasonal prediction skill for the SST anomalies over the tropical Pacific domain is significantly improved in the new version of the model. Because the oceanic memory is retained up to several months, the oceanic states including climatological thermocline depth in the hindcast experiments is not as shallow as that in the free integrations. Therefore, the ENSO magnitude is also predicted realistically in the revised version of the CGCM. On the other hand, ENSO in the hindcast experiment using V1 quickly damps, which lowers the predictability of ENSO in V1.

This study gives some clues to understand the relationship between the simulation fidelity and the prediction skill of ENSO. In case of the ocean, the predicted fields contain the memory of the initial conditions to some extent. Therefore, the oceanic characteristics are maintained as observed in the hindcast experiments for up to several months. In contrast, the predicted atmospheric fields quickly converge to the inherent characteristics of the model due to the short memory of the atmosphere. It implies that the atmospheric simulation in the hindcast experiment is similar to that in the free integrations, while the similarity of simulated oceanic fields between simulation fidelity and the prediction is blurred.

In this study, the simulation of climatology and the ENSO is investigated using two different versions of the model, and possible linkage between the performance of free integrations and seasonal prediction skill is tried to be discussed. Even though some possible linkage between them is presented in this study, however, there is a limitation that the comparison of model performance and seasonal predictability is performed with two climate models.

Fig. 15 **a** Climatological thermocline depth over 160°E–90°W, 5°S–5°N (unit: m) and **b** regressed zonal wind stress anomaly over 160°E–150°W, 5°S–5°N onto Nino3.4 index (unit: N/m^2/°C) in observations (ERA40, *black solid line*), hindcast experiments using the V1 (V2) (*blue* (*red*) *solid line*), and free integrations using the V1 (V2) (*blue* (*red*) *dashed line*)

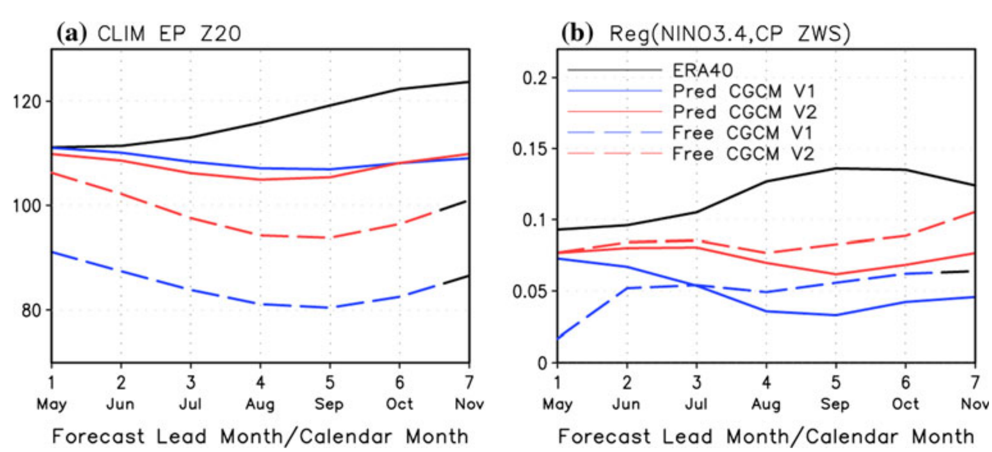

Therefore, further studies should be followed in this line with seasonal prediction experiments multiple numbers of climate models.

Acknowledgments ISK was supported by the National Research Foundation of Korea (NRF) Grant Funded by the Korean Government (MEST) (NRF-2009-C1AAA001-2009-0093042) and second phase of the Brain Korea 21. And, DK was supported by NASA grant NNX09AK34G.

References

AchutaRao K, Sperber K (2002) Simulation of the El Niño Southern Oscillation: results from the coupled model intercomparison project. Clim Dyn 19:191–209. doi:10.1007/s00382-001-0221-9

AchutaRao K, Sperber K (2006) ENSO simulation in coupled ocean-atmosphere models: are the current models better? Clim Dyn 27:1–15. doi:10.1007/s00382-006-0119-7

An S-I, Jin F-F (2001) Collective role of thermocline and zonal advective feedbacks in the ENSO mode*. J Clim 14:3421–3432

An S-I, Wang B (2000) Interdecadal change of the structure of the ENSO mode and its impact on the ENSO frequency. J Clim 13:2044–2055

An S-I, Jin F-F, Kang I-S (1999) The role of zonal advection feedback in phase transition and growth of ENSO in the Cane–Zebiak model. J Meteor Soc Jpn 77:1151–1160

An S-I, Kug J-S, Ham Y-G, Kang I-S (2008) Successive modulation of ENSO to the future greenhouse warming. J Clim 21:3–21

Barnston AG, He Y, Michael HG (1999) Predictive skill of statistical and dynamical climate models in SST forecasts during the 1997–98 El Niño Episode and the 1998 La Niña Onset. Bull Am Meteor Soc 80:217–243

Behringer DW, Xue Y (2004) Evaluation of the global ocean data assimilation system at NCEP: The Pacific Ocean. In: Eighth symposium on integrated observing and assimilation systems for atmosphere, ocean and land surface, AMS 84th annual meeting, Washington State Convention and Trade Center, Seattle, Washington, pp 11–15

Bejarano J, Jin F-F (2006) Coexistence of equatorial coupled modes of ENSO. J Clim 21:3051–3067

Bonan GB (1996) A land surface model (LSM version 1.0) for ecological, hydrological, and atmospheric studies: technical description and user's guide. NCAR Techical Note NCAR/TN-417 + STR, National Center For Atmospheric Research Boulder, Colorado, pp 1–150

Cane MA, Munnich M, Zebiak SE (1990) A study of self-excited oscillations of the tropical ocean–atmosphere system. Part I: Linear analysis. J Atmos Sci 47:1562–1577

Danabasoglu G, Large WG, Tribbia JJ, Gent PR, Briegleb BP, McWilliams JC (2006) Diurnal coupling in the tropical oceans of CCSM3. J Clim 19:2347–2365

Davey M, Huddleston M, Sperber K, Braconnot P, Bryan F, Chen D, Colman R, Cooper C, Cubasch U, Delecluse P et al (2002) STOIC: a study of coupled model climatology and variability in tropical ocean regions. Clim Dyn 18:403–420. doi:10.1007/s00382-001-0188-6

Guilyardi E et al (2009a) Understanding El Niño in ocean-atmosphere general circulation models: progress and challenges. Bull Am Meteor Soc 90:325–340

Guilyardi E, Braconnot P, Jin F-F, Kim ST, Kolasinski M, Li T, Musat I (2009b) Atmosphere feedbacks during ENSO in a coupled GCM with a modified atmospheric convection scheme. J Clim 22:5698–5718

Ham Y-G, Kug J-S, Kang I-S, Jin F-F, Timmermann A (2009) Impact of diurnal atmosphere-ocean coupling on tropical climate simulations using a coupled GCM. Clim Dyn 34, doi:10.1007/s00382-009-0586-8

Hayes SP, Mangum' LJ, PiCaut J, Sumi A, Takeuchi K (1991) TOGA-TAO: a moored array for real-time measurements in the tropical pacific ocean. Bull Am Meteor Soc 72:339–347

Hoffman RN, Kalnay E (1983) Lagged averaged forecasting, an alternative to Monte Carlo forecasting. Tellus 35A:100–118

Holtslag AAM, Boville BA (1993) Local versus nonlocal boundary layer diffusion in a global climate model. J Clim 6:1642–1825

Jin F-F (1997) An equatorial ocean recharge paradigm for ENSO. Part I: Conceptual model. J Atmos Sci 54:811–829

Jin F-F, An S-I (1999) Thermocline and zonal advective feedbacks within the equatorial ocean recharge oscillator model for ENSO. Geophys Res Lett 26(19):2989–2992, doi:10.1029/1999GL002297

Jin EK, Kinter JL, Wang B, Park C-K, Kang I-S, Kirtman BP, Kug J-S, Kumar A, Luo J-J, Schemm J et al (2008) Current status of ENSO prediction skill in coupled ocean–atmosphere models. Clim Dyn 31:647–664. doi:10.1007/s00382-008-0397-3

Kang I-S, Kug J-S (2002) El Nino and La Nina sea surface temperature anomalies: asymmetry characteristics associated with their wind stress anomalies. J Geophys Res 107(D19):4372

Kessler WS, Kleeman R (2000) Rectification of the Madden–Julian Oscillation into the ENSO Cycle. J Clim 13:3560–3575

Kim D, Kug J-S, Kang I-S, Jin F-F, Wittenberg A (2008) Tropical Pacific impacts of convective momentum transport in the SNU coupled GCM. Clim Dyn 31, doi:10.1007/s00382-007-0348-4

Kirtman BP (1997) Oceanic Rossby wave dynamics and the ENSO period in a coupled model. J Clim 10:1690–1704

Kirtman BP, Shukla J, Balmaseda M, Graham N, Penland C, Xue Y, Zebiak SE (2001) Current status of ENSO forecast skill: A report to the Climate Variability and Predictability (CLIVAR) Working Group on Seasonal to Interannual Prediction. WCRP Informal Report No 23/01, p. 31

Kug J-S, Kang I-S, An S-I (2003) Symmetric and antisymmetric mass exchanges between the equatorial and off-equatorial Pacific associated with ENSO. J Geophys Res 108(C8):3284

Kug J-S, Kang I-S, Choi D-H (2008) Seasonal climate predictability with Tier-one and Tier-two prediction systems. Clim Dyn 31, doi:10.1007/s00382-007-0264-7

Kug J-S, Choi J, An S-I, Jin F-F, Wittenberg AT (2010) Warm pool and cold tongue El Nino events as simulated by the GFDL 2.1 coupled GCM. J Clim 23:1226–1239

Large WG, Gent PR (1999) Validation of vertical mixing in an equatorial ocean model using large eddy simulations and observations. J Phys Oceanogr 29:449–464

Latif M, Sperber K, Arblaster J, Braconnot P, Chen D, Colman A, Cubasch U, Cooper C, Delecluse P, Dewitt D et al (2001) ENSIP: the El Niño simulation intercomparison project. Clim Dyn 18:255–276. doi:10.1007/s003820100174

Le Treut H, Li Z-X (1991) Sensitivity of an atmospheric general circulation model to prescribed SST changes: feedback effects associated with the simulation of cloud optical properties. Clim Dyn 5:175–187

Lee M-I, Kang I-S, Kim J-K, Mapes BE (2001) Influence of cloud-radiation interaction on simulating tropical intraseasonal oscillation with an atmospheric general circulation model. J Geophys Res 106:14219–14233

Lee M-I, Kang I-S, Mapes BE (2003) Impacts of cumulus convection parameterization on aqua-planet AGCM simulations of tropical intraseasonal variability. J Meteor Soc Jpn 81:963–992

Lin J-L (2007) The double-ITCZ problem in IPCC AR4 coupled GCMs: ocean–atmosphere feedback analysis. J Clim 20:4497–4525

Lin J-L, Lee M-I, Kim D, Kang I-S, Frierson DMW (2008) The impacts of convective parameterization and moisture triggering on AGCM-simulated convectively coupled equatorial waves. J Clim 21:883–909

Luo J-J, Masson S, Behera S, Shingu S, Yamagata T (2005) Seasonal climate predictability in a coupled OAGCM using a different approach for ensemble forecasts. J Clim 18:4474–4497

McPhaden MJ (1999) Genesis and evolution of the 1997–98 El Niño. Science 283:950–954

McPhaden MJ (2002) Mixed layer temperature balance on intraseasonal timescales in the Equatorial Pacific Ocean*. J Clim 15:2632–2647

McPhaden MJ, Taft BA (1988) Dynamics of seasonal and intraseasonal variability in the Eastern Equatorial Pacific. J Phys Oceanogr 18:1713–1732

Nakajima T, Tsukamoto M, Tsushima Y, Numaguti A (1995) Modelling of the radiative processes in an AGCM. In: Matsuno T (ed) Climate system dynamics and modelling, vol 1–3. University of Tokyo, Tokyo, pp 104–123

Neale RB, Richter JH, Jochum M (2008) The impact of convection on ENSO: from a delayed oscillator to a series of events. J Clim 21:5904–5924

Noh Y, Kim HJ (1999) Simulations of temperature and turbulence structure of the oceanic boundary layer with the improved near-surface process. J Geophys Res 104:15621–15634

Numaguti A, Takahashi M, Nakajima T, Sumi A (1995) Development of an atmospheric general circulation model. In: Matsuno T (ed) Climate system dynamics and modelling. Univrsity of Tokyo, Tokyo, vol I–3, pp 1–27

Seiki A, Takayabu YN (2007) Westerly wind bursts and their relationship with intraseasonal variations and ENSO. Part I: statistics. Mon Weather Rev 135:3325–3345

Smith T, Reynolds R (2004) Improved extended reconstruction of SST (1854–1997). J Clim 17:2466–2477

Sooraj KP, Kim D, Kug J-S, Yeh S-W, Jin F-F, Kang I-S (2008) Effects of the low frequency zonal wind variation on the high frequency atmospheric variability over the tropics. Clim Dyn 33:496–507. doi:10.1007/s00382-008-0483-6

Tiedtke M (1983) The sensitivity of the time-mean large-scale flow to cumulus convection in the ECMWF model. Workshop on Convection in large-scale numerical models. ECMWF, 28 Nov–1 Dec 1983, pp 297–316

Tokioka T, Yamazaki K, Kitoh A, Ose T (1988) The equatorial 30–60 day oscillation and the Arakawa-Schubert penetrative cumulus parameterization. J Meteor Soc Jpn 66:883–901

Uppala SM et al (2005) The ERA-40 re-analysis. Quart J R Meteorol Soc 131:2961–3012. doi:10.1256/qj.04.176

Vecchi GA, Harrison DE (2000) Tropical Pacific Sea surface temperature anomalies, El Niño, and Equatorial Westerly Wind Events*. J Clim 13:1814–1830

Wang B, Lee J-Y, Kang I-S, Shukla J, Park C-K, Kumar A, Schemm J, Cocke S, Kug J-S, Luo J-J et al (2009) Advance and prospectus of seasonal prediction: assessment of the APCC/CliPAS 14-model ensemble retrospective seasonal prediction (1980–2004). Clim Dyn 33:93–117. doi:10.1007/s00382-008-0460-0

Wittenberg AT, Rosati A, Lau NC, Ploshay JJ (2006) GFDL's CM2 global coupled climate models. Part III: Tropical pacific climate and ENSO. J Clim 19:698–722

Wu X, Grabowski WW, Moncrieff MW (1998) Long-term behavior of cloud systems in TOGA COARE and their interactions with radiative and surface processes. Part I: Two-dimensional modeling study. J Atmos Sci 55:2693–2714

Wu X, Deng L, Song X, Vettoretti G, Peltier WR, Zhang GJ (2007) Impact of a modified convective scheme on the Madden-Julian Oscillation and El Niño-Southern Oscillation in a coupled climate model. Geophys Res Lett 34:L16823

Xie P, Arkin PA (1997) Global precipitation: a 17-year monthly analysis based on gauge observations, satellite estimates, and numerical model outputs. Bull Am Meteor Soc 78:2539–2558

Yeh S-W, Kug J-S, Dewitte B, Kwon M-H, Kirtman B, Jin F-F (2009) El Niño in a changing climate. Nature 461:511–514

Zeng X, Zhao M, Dickinson RE (1998) Intercomparison of bulk aerodynamic algorithms for the computation of sea surface fluxes using TOGA COARE and TAO data. J Clim 11:2628–2644